Mutual Enhancement of Wind- and Tide-Induced Near-Inertial Internal Waves in Luzon Strait

ZHIWU CHEN,[a,b] GENGBIN LIU,[a,c] ZHIYU LIU,[d] SHAOMIN CHEN,[a,c] HUAIHAO LU,[a,c] JIEXIN XU,[a,b] YANKUN GONG,[a,b] JIESHUO XIE,[a,b] YINGHUI HE,[a,b] JU CHEN,[a,b,e] YUNKAI HE,[a,b,e] AND SHUQUN CAI[a,b,f]

[a] *State Key Laboratory of Tropical Oceanography, South China Sea Institute of Oceanology, Chinese Academy of Sciences, Guangzhou, China*
[b] *Southern Marine Science and Engineering Guangdong Laboratory (Guangzhou), Guangzhou, China*
[c] *University of Chinese Academy of Sciences, Beijing, China*
[d] *State Key Laboratory of Marine Environmental Science, and Department of Physical Oceanography, College of Ocean and Earth Sciences, Xiamen University, Xiamen, China*
[e] *Xisha Marine Environmental National Observation and Research Station, Sansha, China*
[f] *Institution of South China Sea Ecology and Environmental Engineering, Chinese Academy of Sciences, Guangzhou, China*

(Manuscript received 2 March 2022, in final form 9 August 2022)

ABSTRACT: Tide-induced near-inertial internal waves (NIWs) are generated by tide–topography interaction and are energized by internal tides through triadic resonant interaction of internal waves. They are located above topography and could be in close contact with wind-induced NIWs when the topography is a tall ridge, like in the Luzon Strait of the northern South China Sea (SCS). A natural question arises as to whether there is significant interaction between wind- and tide-induced NIWs. By using moored velocity observations, a satellite-tracked surface drifter dataset, and idealized numerical simulations, we find that in the presence of tide-induced NIWs, the wind can inject slightly more near-inertial energy (NIE), while in the presence of wind-induced NIWs, significantly more tidal energy is transferred to NIWs. Thus, wind- and tide-induced NIWs can mutually enhance each other, producing more NIE than a linear superposition of that generated by wind and tide forcing alone. Increasing wind intensity and tidal excursion lead to saturation of NIE enhancement, while a taller ridge leads to stronger enhancement. The high mixed layer NIE near Luzon Strait is mostly generated by the wind, while the mutual enhancement between wind- and tide-induced NIWs can further enhance this pattern. The interaction between wind- and tide-induced NIWs leads to an enhancement of 25% more NIE. If tide-induced NIWs are neglected, as is usually the case in the estimation of NIE, the total NIE will be underestimated by almost 50%. This might imply that tide-induced NIWs are important for the energetics of NIWs in Luzon Strait.

SIGNIFICANCE STATEMENT: Near-inertial internal waves (NIWs) usually occupy the most kinetic energy of internal waves and contribute significantly to ocean mixing. Near the surface they are usually generated by wind forcing, but near the bottom they can be generated by geostrophic or tidal flow interacting with topography. Above the tall ridge in Luzon Strait, wind- and tide-induced NIWs are in close contact, leading to potential interactions. It is found that these NIWs can mutually enhance each other, with most of the additional near-inertial energy (NIE) coming from the tides. If tide-induced NIWs are neglected, the total NIE will be underestimated by almost 50%. This suggests that tide-induced NIWs are important for the energetics of NIWs in Luzon Strait.

KEYWORDS: Inertia-gravity waves; Instability; Internal waves

1. Introduction

Near-inertial internal waves (NIWs) usually occupy the most kinetic energy in the internal wave field; e.g., there is a prominent peak near the local inertial frequency in the quasi-universal Garrett–Munk (GM) spectrum (Munk 1981). NIWs usually possess high vertical shear and are thus conducive to shear instabilities, inducing turbulent dissipation and mixing. They are regarded to provide a significant portion of the mechanical energy required to maintain the global meridional overturning circulation. Their generation mechanisms include wind forcing (Pollard and Millard 1970; D'Asaro 1985; Zhai et al. 2007), spontaneous emission through loss of balance (Vanneste 2013; Nagai et al. 2015), nonlinear wave–wave interactions (Müller et al. 1986; Hibiya et al. 2002; MacKinnon and Winters 2005), and breaking lee waves over topography (Nikurashin and Ferrari 2010; Hu et al. 2020; Zemskova and Grisouard 2021). By far, the wind forcing mechanism has received the most observational support, but the relative importance of the other mechanisms is not known. A recent review was given by Alford et al. (2016).

Similar to the breaking lee wave mechanism, breaking internal tides over topography can also generate NIWs. Lamb (2004) showed this in his simulations of tide–topography interaction, although it was not the subject pursued therein. Nikurashin and Legg (2011) detailed this process, in which the breaking of internal tides initiates the generation of NIWs. These NIWs (f) then interact with internal tides (ω)

Corresponding authors: Shuqun Cai, caisq@scsio.ac.cn; Jiexin Xu, manglo.xu@163.com

DOI: 10.1175/JPO-D-22-0055.1

to produce a triadic (f, $\omega - f$, ω) resonant interaction, and then internal tide energy is continuously transferred to NIWs. This resonant triad is slightly different from that in parametric subharmonic instability (PSI; see, e.g., Müller et al. 1986) of internal tides, in which the two subharmonic frequencies are equal to one-half of the parent wave frequency ω. The consequence is that PSI of internal tides can generate NIWs only at the critical latitude (e.g., 28.9° for M_2 internal tides), while the more general resonant triad (f, $\omega - f$, ω) can generate NIWs in a much broader latitude range. From in situ observations in the northern South China Sea (~20°N), Xie et al. (2011) observed the generation of NIWs by this more general resonant triad. Recently, Wang et al. (2021a,b) numerically investigated this resonant triad interaction over midocean ridges and also the influences of background geostrophic currents.

One remarkable result of Nikurashin and Legg (2011) is that their simulation produced a continuum kinetic energy frequency spectrum indistinguishable in shape from that of the GM spectrum. Liang and Wunsch (2015) commented that this might be the first time a full, realistic internal wave continuum was produced in a numerical simulation. By using a numerical model, Sugiyama et al. (2009) argued that both wind and tide forcings are necessary to generate a GM-like spectrum. These two forcings generate NIWs and internal tides, respectively, which then interact with each other to develop a full GM-like spectrum. Since NIWs can now be generated by tide–topography interaction (referred to as tide-induced NIWs hereinafter), Chen et al. (2019) showed that tidal forcing alone is sufficient to generate a GM-like spectrum (in the sense that there is a prominent near-inertial peak and that the spectral slope in log–log coordinates is close to −2 at high frequencies). The implication is that the observed GM spectrum in the deep ocean (i.e., in the absence of wind forcing) is likely due to tidal forcing alone. Steady geostrophic flow interacting with bottom topography can generate lee waves, whose breaking may also lead to the appearance of NIWs (Nikurashin and Ferrari 2010; Hu et al. 2020; Zemskova and Grisouard 2021), but this is not the subject pursued in the present study.

Tide-induced NIWs exist above topography. For a tall ridge with strong tides, like in Luzon Strait of the northern South China Sea (SCS), tide-induced NIWs are in close contact with wind-induced NIWs. A natural question arises: can wind- and tide-induced NIWs enhance or attenuate each other? Is there any interaction between these NIWs of different origins? These questions provide direct motivation for the present study. Interaction between wind and tide has also been considered by Xing and Davies (1997, 2002) and very recently by Omidvar et al. (2022), but these studies mainly focus on the shelf edge or nearshore region where the water depth is shallow and wind-induced upwelling is strong. The interaction mainly produces energy at the sum of f and M_2 frequency (Xing and Davies 2002) or influences the internal tide generation process (Omidvar et al. 2022).

By using moored velocity observations, drifter observations, and numerical simulations, it will be shown in the present work that wind- and tide-induced NIWs can mutually enhance each other, producing a resonant-like effect. Section 2 presents the data and methods used for the analysis. Section 3 presents detailed energy budget calculations to show the mutual enhancement between wind- and tide-induced NIWs. The effects of winds, tides, and topography are explored, and the high mixed layer near-inertial energy (NIE) near Luzon Strait is discussed. Finally, the conclusions are summarized in section 4.

2. Data and methods

a. Moored velocity observations

A mooring was deployed at 20.5°N, 120.5°E from 15 July 2017 to 26 August 2018 near Luzon Strait in the northern SCS (the white star in Fig. 10a). The local water depth is 3289 m. Upward- and downward-looking acoustic Doppler current profilers (ADCPs) were placed near a depth of 600 m, with a sampling interval of 1 h and a vertical resolution of 8 m. Unfortunately, the downward-looking ADCP was broken and thus only current data from the upward-looking ADCP (data from 100- to 596-m depth) are used for analysis.

b. Global Drifter Program dataset

The Global Drifter Program (GDP, https://www.aoml.noaa.gov/phod/gdp/hourly_data.php) dataset provides hourly velocity records at 15-m depth (Elipot et al. 2016). These velocity data are derived from the raw locations of satellite-tracked surface drifters at irregular time intervals (roughly 1.2 h on average) and then interpolated onto the regular hourly time grids. For the region considered in this study (108°–126°E, 10°–27°N, Fig. 10a), the data span from 2003 to 2018. Drifters with lifetimes shorter than 300 h or breaking times longer than 10 h are discarded. This results in 1 100 491 out of 1 308 226 velocity records being retained. The missing values are filled by linear interpolation.

These velocity data are then used for computing the mixed layer NIE. As the inertial frequency f varies along drifter trajectories, velocity records tracked by a drifter are broken into half-overlapping 300-h segments. Then, f is set as the mean value over each segment and a bandpass filter is applied to extract the near-inertial velocities u_i and v_i. This procedure for extracting u_i and v_i from the GDP dataset is the same as that in Liu et al. (2019). Temperature data from the *World Ocean Atlas 2018* (*WOA2018*) are used for calculating the mixed layer depth D, which is defined as the depth where the temperature is 0.5°C lower than the mean temperature of the surface 10-m layer.

c. Numerical modeling

An idealized 2D (x, z) model is utilized to study the impacts of both wind and tide. It consists of a single Gaussian ridge [$h(x) = h_0\exp(-x^2/2L^2) - H$, with $h_0 = 2.2$ km, $L = 12$ km, and $H = 3$ km] representing the eastern ridge in Luzon Strait of the northern SCS along the 20.5°N transect (the magenta line in Fig. 10a). The upper boundary at $z = 0$ m is a free surface, where time variable zonal wind stress (from 1 January to 1 March 2018, 60 days in total) from the hourly NCEP CFSv2 (https://www.hycom.org/dataserver/ncep-cfsv2) is applied. Barotropic tide $u = u_0\sin(\omega t + \phi_0)$ is applied at the

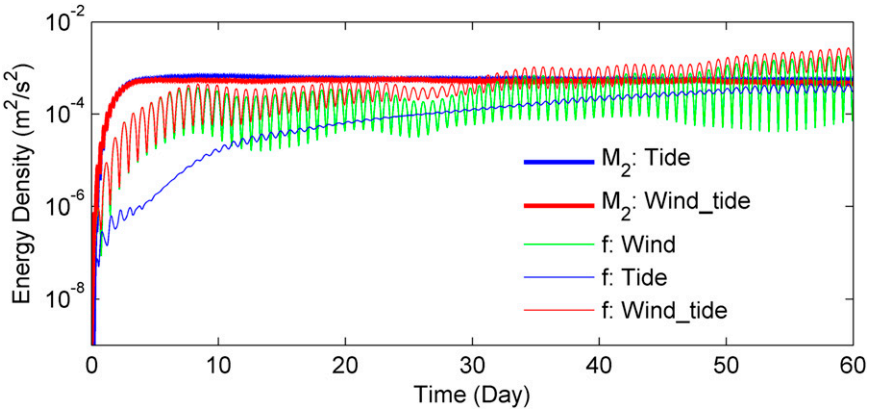

FIG. 1. Time evolution of M_2 (thick lines) and near-inertial (thin lines) energy density averaged between $-400 \le x \le 40$ km for cases Wind, Tide, and Wind_tide.

eastern open boundary, with tidal amplitude $u_0 = 0.06$ m s^{-1}, M_2 tidal frequency $\omega = 1.41 \times 10^{-4}$ rad s^{-1}, and the initial tidal phase $\phi_0 = 0$. The buoyancy frequency profile is shown at the right-hand side of Fig. 2a, with $N_0 = 0.002$ and $N_1 = 0.012$ rad s^{-1}. The local Coriolis frequency is $f = 5 \times 10^{-5}$ rad s^{-1}. According to Garrett and Kunze (2007), the three nondimensional parameters governing the generation of internal tides are the steepness parameter $\varepsilon = \max[h_x/\sqrt{(\omega^2 - f^2)/(N_0^2 - \omega^2)}] = 1.7$, the tidal excursion parameter $ku_0/\omega = 0.22$ (where $k = 2\pi/L$), and $N_0 h_0/u_0 = 73.3$. In later section, u_0, h_0, and L will be varied in sensitivity analysis simulations, with ku_0/ω and $N_0 h_0/u_0$ varying in the ranges of [0.04, 0.34] and [49, 440], respectively, while ε remaining unchanged.

The MITgcm (Marshall et al. 1997) is utilized for simulations. A uniform horizontal grid spacing $\Delta x = 100$ m is adopted within $-400 \le x \le 40$ km (Figs. 2a–c). It is then gradually stretched both eastward and westward to $\Delta x = 3$ km and then kept fixed until the boundaries at $x = \pm 900$ km. Near both boundaries, a sponge layer with 40 grid points is implemented to avoid wave reflections. In the vertical direction, $\Delta z = 3$ m in the upper 300 m. It is then gradually stretched downward to $\Delta z = 18$ m and then kept fixed until the no-slip bottom boundary. The simulations are carried out in a hydrostatic mode, using the nonlocal KPP scheme (Large et al. 1994) for vertical mixing. The background vertical viscosity and diffusivity are $\nu_v = \kappa_v = 10^{-5}$ m^2 s^{-1} and the horizontal ones are $\nu_h = \kappa_h = 10^{-2}$ m^2 s^{-1}. When the nonhydrostatic mode is turned on with constant viscosities and diffusivities ($\nu_v = \kappa_v = 10^{-4}$ m^2 s^{-1} and $\nu_h = \kappa_h = 10^{-2}$ m^2 s^{-1}), the high-frequency part of the internal wave continuum is enhanced, but the change in NIE is negligible. This is presumably because near-inertial motions are mainly in the horizontal direction and thus the nonhydrostatic effect is weak. Since NIWs are the focus of the present work, hydrostatic simulations are performed for computation efficiency. All simulations are initiated from a state of rest and run for two months (60 days), with a time step of $\Delta t = 5$ s.

It should be noted that even though the model is nominally 2D (x, z), it actually also solves the y-momentum equation with the condition that there is no variation along the y direction (i.e., $\partial/\partial y = 0$). Thus, the model result also includes the v-velocity component, and this allows NIWs to develop. This model configuration has been utilized in existing literatures for the simulation of NIWs, e.g., Tort and Winters (2018). The above detailed model setups are basically the same as those in Chen et al. (2019) for the study of NIWs and internal wave spectra.

3. Results and discussion

a. *Enhancement of near-inertial energy*

When the model is forced by wind alone (case Wind), tide alone (case Tide), and combined wind and tide (case Wind_tide), time evolutions of the bandpass filtered M_2 internal tide energy (0.85–1.15M_2) and NIE (0.85–1.15f) are shown in Fig. 1. The M_2 internal tide energy quickly approaches steady state and there is not much difference between cases Tide and Wind_tide. The NIE in cases Wind and Wind_tide becomes steady earlier than that in case Tide, in which the NIE finally approaches the same magnitude as the tidal energy. After day 25, there is a slight increasing trend of NIE in both Wind and Wind_tide, possibly due to the slightly intensifying wind stress. The spatial distributions of NIE averaged in the last 30 days of simulations for cases Wind, Tide, and Wind_tide are shown in Figs. 2a–2c, respectively. In Fig. 2a, NIE is mainly distributed in the upper 100 m, consistent with the characteristics of wind-induced NIWs. In Fig. 2b, NIE appears above the ridge top and decreases away from the ridge. This is because internal tide breaking above the ridge leads to self-adjustment of the rotating ocean, which initiates the generation of NIWs. These waves (f) then interact with the internal tides (M_2) to produce a triadic (f, $M_2 - f$, M_2) resonant interaction, and then tidal energy is continuously transferred to the NIWs. This process has been detailed in Nikurashin and Legg (2011) and Chen et al. (2019), and the consequence is that a GM-like (in the sense that there is a prominent near-inertial peak in the frequency spectrum and that the spectral slope in log–log coordinates is close to -2 at high frequencies) internal wave spectrum can be generated by tidal forcing alone (Chen et al. 2019). In Fig. 2c, NIE is much enhanced in the whole water column.

Comparison of NIE profiles between mooring and model results is shown in Fig. 2d. The black solid line is calculated by a 30-day segment of the mooring observation starting from

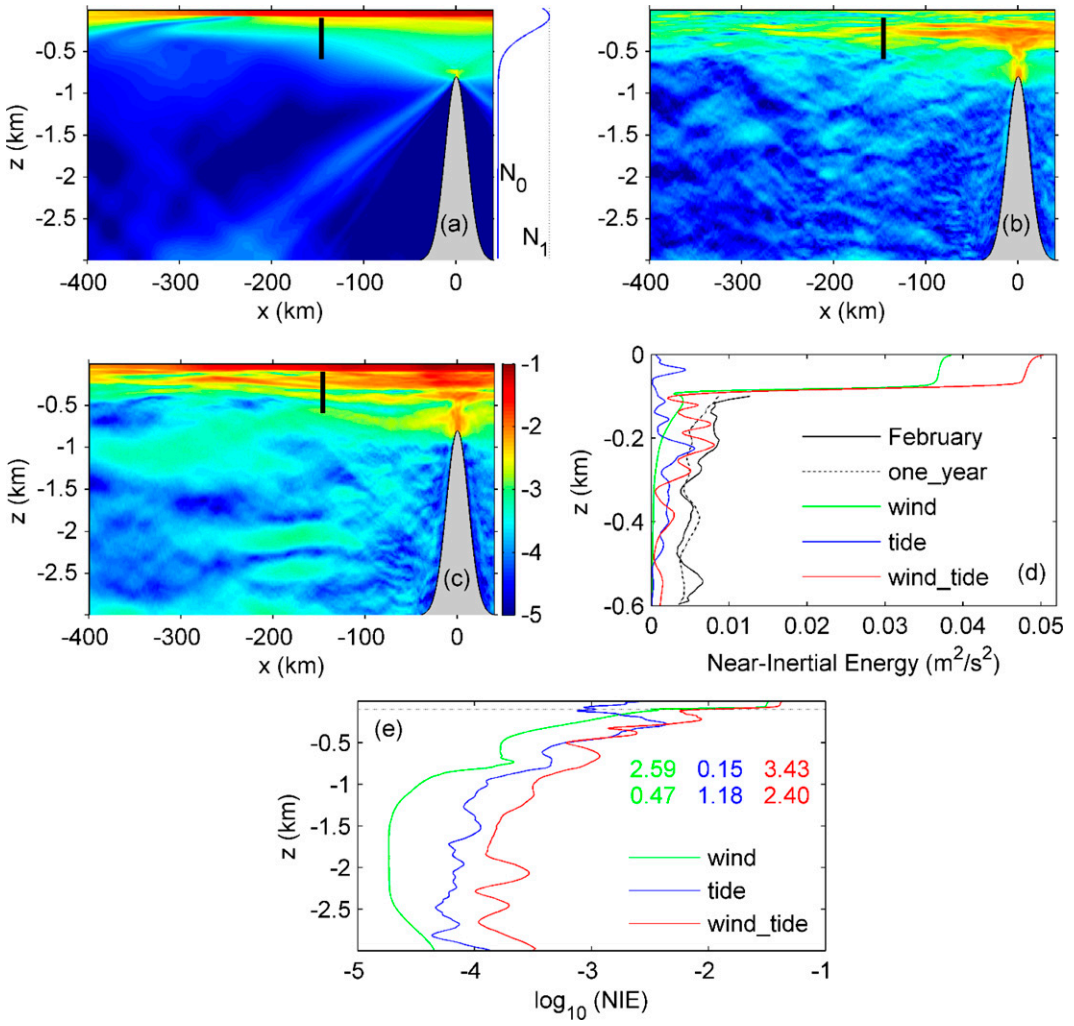

FIG. 2. Logarithm of NIE ($m^2\ s^{-2}$) for cases (a) Wind, (b) Tide, and (c) Wind_tide, with the buoyancy frequency profile shown at the right-hand side of (a). (d) NIE profiles from both mooring (black solid and dotted lines) and model results (green, blue, and red lines), with the mooring position indicated by the thick black line in (a)–(c). (e) Vertical profiles of the horizontally averaged NIE in (a)–(c). The upper and lower rows of numbers ($m^3\ s^{-2}$) indicate vertical integration of the corresponding profiles (with the same color) above and below the mixed layer depth (gray dashed line), respectively.

1 February 2018 (the same period as that of the wind applied in the model). The whole time series from the mooring is also computed for comparison (dotted line). In the upper 100 m, NIE is mainly generated by the wind and its value in case Wind_tide is apparently larger than a linear superposition of its values in cases Wind and Tide. Below 100-m depth, NIE in case Wind decreases smoothly and the vertically oscillatory structure in case Wind_tide is due to tide-induced NIWs. Apparently, of the three model results, case Wind_tide (red line) is the closest to the observation (black solid line). The depth-averaged (in the depth range of the observation) NIEs for cases Wind, Tide, Wind_tide, and the observation (black solid line) are 6.8×10^{-4}, 1.7×10^{-3}, 2.7×10^{-3}, and 5.9×10^{-3} $m^2\ s^{-2}$, respectively. However, the most striking result is that, by visual inspection, the vertical oscillation of NIE (red line) follows the same oscillatory phase as that of the observed one (black solid line), even though the former is systematically smaller than the latter. Note that the model is not tuned in any way to match the observation. By close inspection, NIE from the whole observation period (dotted line) also possesses a vertically oscillatory structure that closely follows the same oscillatory phase as those of the red and black solid lines. This shows that this vertically oscillatory structure is robust in observation, and it provides an observational support to the persistent existence of tide-induced NIWs.

Vertical profiles of NIE horizontally averaged between $-400 \le x \le 40$ km from the three model cases are shown in Fig. 2e, with values of vertical integrations above and blow the mixed layer depth indicated. In case Wind, 85% of the NIE

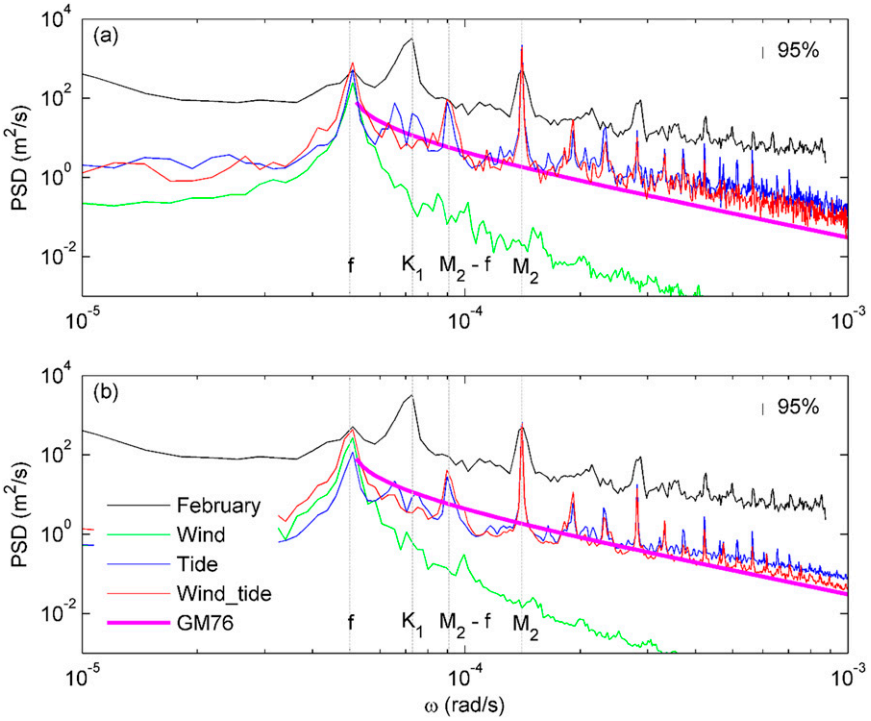

FIG. 3. Power spectral density from both mooring (vertically averaged; the short vertical bar indicates the 95% confidence interval with 40 degrees of freedom) and model results, as compared to the GM76 spectrum. The observed (black line) and GM76 (thick magenta line) spectra are the same in both (a) and (b), while the model spectra are (a) vertically averaged as in the observation and (b) domain averaged between $-400 \le x \le 40$ km. Panel (a) shares the same legend as in (b).

resides in the mixed layer, while in case Tide 89% resides below the mixed layer. With the simultaneous presence of wind- and tide-induced NIWs in case Wind_tide, NIEs in and below the mixed layer are of comparable magnitude (3.43 versus 2.40 $m^3\ s^{-2}$). Also, it is apparent that, both in and below the mixed layer, NIE in case Wind_tide is larger than the linear superposition of those in cases Wind and Tide, which will be discussed in detail later.

Power spectral density (PSD) from both mooring observation (February) and model results are shown in Fig. 3. The corresponding GM76 spectrum (calculated using the MATLAB toolbox created by J. Klymak, http://jklymak.github.io/GarrettMunkMatlab/) is also plotted for comparison. Overall, the model spectra vertically averaged as in the observation (Fig. 3a) are one to two orders of magnitude lower than the observed one. Being in a region of active mesoscale eddy activity (e.g., Zhang et al. 2017), the observation also has high subinertial energy and an overall higher background energy than the model results, which do not include diurnal tides, mesoscale eddies, other complicated background currents, etc. The model spectra domain averaged between $-400 \le x \le 40$ km (Fig. 3b) are qualitatively the same as those in Fig. 3a, but smoother, especially in the high-frequency part. The dominant peaks in observation are due to diurnal (K_1) and semidiurnal (M_2) internal tides. There is also a significant peak near f. Since the observation only covers the depth below 100 m and considering the vertically oscillatory structure shown in Fig. 2d, this near-inertial peak very likely corresponds to tide-induced NIWs. For case Tide, a prominent near-inertial peak appears, corresponding to tide-induced NIWs that have been discussed extensively by Chen et al. (2019). The underlying mechanism is that the three frequencies (f, $M_2 - f$, M_2) form a resonant triad to continuously transfer internal tide energy into NIWs. For K_1 internal tide, the subharmonic wave frequency $K_1 - f$ is smaller than f (i.e., not in the freely propagating internal wave regime) and thus the energy transfer from K_1 internal tide into NIWs is damped. This is why it is not K_1, but M_2, internal tide that is applied in the model, even though K_1 is much stronger than M_2 in the observation. For case Wind, the near-inertial peak is higher than that in case Tide, but the high-frequency part has much lower energy. For case Wind_tide, the simultaneous presence of wind and tide forcings produces a much stronger near-inertial peak (Fig. 3b). It should be noted that the $M_2 - f$ peak is an order of magnitude weaker than the f peak, and this might be why it is difficult to be captured in a complex background by the observation. Sometimes a small $M_2 - f$ peak could be observed near Luzon Strait, e.g., see Fig. 1b in Xie et al. (2011).

The domain averaged NIE densities $[0.5\rho_0(u_i^2 + v_i^2)$, where $\rho_0 = 1025\ kg\ m^{-3}]$ for cases Wind (NIE_w), Tide (NIE_t), and

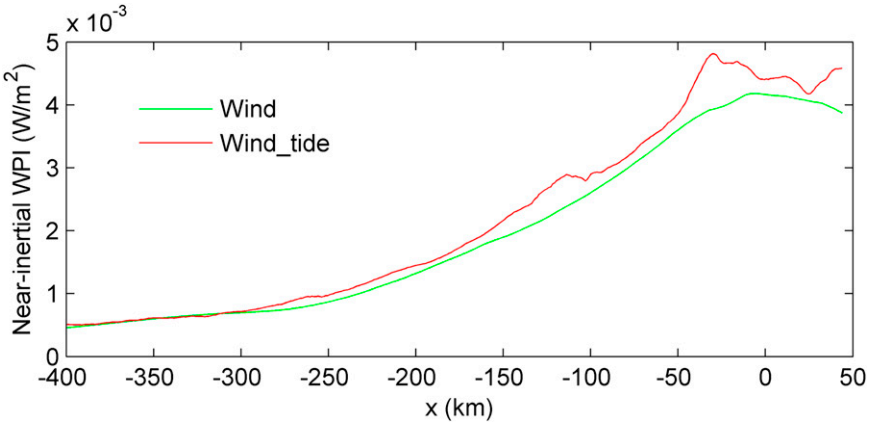

FIG. 4. Spatial distribution of time-averaged near-inertial Wind Power Input (WPI) for cases Wind and Wind_tide.

Wind_tide (NIE_{wt}) are 1.10, 0.47, and 2.08 J m^{-3}, respectively. It seems that the interaction between wind- and tide-induced NIWs leads to an enhancement of NIE. To quantify such interaction, we define two ratios

$$R_1 = (NIE_{wt} - NIE_w - NIE_t)/NIE_{wt}, \quad \text{and} \tag{1}$$

$$R_2 = (NIE_{wt} - NIE_w)/NIE_{wt}, \tag{2}$$

where the subscripts w, t, and wt denote the cases Wind, Tide, and Wind_tide, respectively. Thus, $R_1 = 0.25$, indicating that the interaction can lead to an enhancement of 25% more NIE. $R_2 = 0.47$, indicating that the total NIE will be underestimated by 47% if tide-induced NIWs are neglected. This highlights the importance of tide-induced NIWs in constraining NIE in Luzon Strait.

b. Energetics

Where does the additional 25% NIE come from? It must come from either the wind or the tide, or both. In the presence of tide-induced NIWs, the surface near-inertial velocity u_i might be modified, and this might change the near-inertial wind power input (WPI)

$$W_i = \tau u_i, \tag{3}$$

where τ is the applied zonal wind stress. The spatial distributions of time-averaged W_i for cases Wind and Wind_tide are shown in Fig. 4. Near the ridge ($x = 0$) where tide-induced NIWs are strong, W_i in case Wind_tide is significantly larger than that in case Wind. Away from the ridge, the difference in W_i between these two cases diminishes. This verifies that the presence of tide-induced NIWs can enhance near-inertial WPI. The instantaneous and cumulative (integration in time from the start of simulations, the same below) near-inertial WPI averaged between $-400 \le x \le 40$ km are shown in Fig. 5 (green and red lines). The instantaneous WPI oscillates between positive and negative values. It has slightly larger magnitude in case Wind_tide than that in case Wind. By the end of simulations, the cumulative wind energy input in case Wind_tide (5.97 J m^{-3}) is 7% larger than that in case Wind (5.53 J m^{-3}). Thus, even though the presence of tide-induced NIWs can enhance near-inertial wind energy input, such effect is pretty weak.

To calculate the energy transfer from internal tides to NIWs, we adopt the energy budget framework of Hazewinkel and Winters (2011), which has also been utilized in many existing literatures to study the energy budget of NIWs in triadic resonant interaction of internal waves (e.g., Onuki and Hibiya 2015; Ansong et al. 2018; Yang et al. 2018; Wang et al. 2021a,b). The flow fields are decomposed as

$$\mathbf{u} = \mathbf{u}_T + \mathbf{u}_s, \quad b = b_T + b_s, \quad p = p_T + p_s, \tag{4}$$

where $\mathbf{u}$ and p are the velocity vector and pressure, respectively; $b = -(g/\rho_0)\rho'$ is buoyancy; g is the gravitational acceleration; and ρ_0 and ρ' are the reference and perturbation densities, respectively. The subscripts T and s denote internal tides and subharmonic waves, which are obtained by high-pass and low-pass filtering, respectively, using a cutoff frequency of $0.8M_2$. This filtering is adopted so that the flow fields can be decomposed into only two parts, which are dominated by internal tides and NIWs, respectively. The energy equation for subharmonic waves is

$$\frac{\partial E_s}{\partial t} + \nabla \cdot \mathbf{F}_s = G - D_s. \tag{5}$$

Note that in the derivation of this equation, the buoyancy frequency $N(z)$ is assumed to vary slowly enough so that terms involving its derivative could be neglected (Hazewinkel and Winters 2011). The energy density is calculated as

$$E_s = \frac{1}{2}\left(u_s^2 + v_s^2 + w_s^2 + \frac{b_s^2}{N^2}\right), \tag{6}$$

while the energy flux is

$$\mathbf{F}_s = \frac{1}{\rho_0}\mathbf{u}_s p_s + \mathbf{u}_T E_s. \tag{7}$$

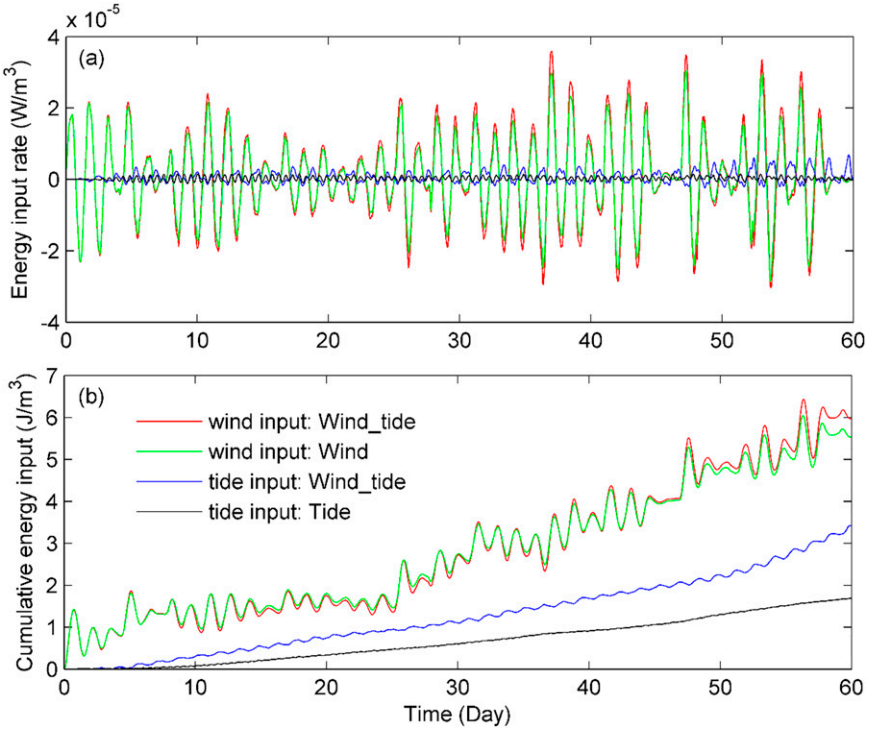

FIG. 5. (a) Instantaneous and (b) cumulative near-inertial energy input from both wind and tide for cases Wind, Tide, and Wind_tide. Panel (a) shares the same legend as in (b).

The energy transfer from internal tides to subharmonic waves (mainly NIWs) is calculated by the transfer term

$$G = -\mathbf{u}_s \cdot (\mathbf{u}_s \cdot \nabla)\mathbf{u}_T - \frac{b_s}{N^2}(\mathbf{u}_s \cdot \nabla)b_T, \tag{8}$$

in which the buoyancy term (the second term) can be neglected and it is the horizontal straining of the tide (the first term) that transfers the energy (MacKinnon and Winters 2005; Young et al. 2008; Hazewinkel and Winters 2011). Thus, the energy transfer term can be simplified as

$$G \approx -u_s u_s \frac{\partial u_T}{\partial x} - u_s v_s \frac{\partial v_T}{\partial x}. \tag{9}$$

The energy dissipation is calculated as

$$D_s = \nu_e \left(\frac{\partial \mathbf{u}_s}{\partial z}\right)^2 + \frac{\kappa_e}{N^2}\left(\frac{\partial b_s}{\partial z}\right)^2, \tag{10}$$

since the horizontal dissipation terms are negligible. The effective viscosity ν_e and diffusivity κ_e are from the KPP parameterization. When volume averaged between $-400 \le x \le 40$ km, the flux divergence term is negligible and the energy balance is dominated by the energy growth [the first term on the left-hand side of Eq. (5)], transfer, and dissipation terms in Eq. (5).

Spatial distributions of the energy transfer rate G [Eq. (9)] time-averaged in the last 30 days of simulations are shown in Fig. 6 for cases Tide and Wind_tide. Positive values denote energy transfer from internal tides to subharmonic waves, while negative values denote the reverse transfer. Since the subharmonic waves mainly consist of NIWs, in the following we refer to G as the energy transfer from internal tides to NIWs, as in Hazewinkel and Winters (2011). In Fig. 6a, the values are mostly positive, which are concentrated along the internal wave beam path and are mostly confined in the upper 500 m depth. With the presence of wind-induced NIWs in Fig. 6b, the positive energy transfer is significantly enhanced, indicating that the presence of wind-induced NIWs can facilitate energy transfer from internal tides to NIWs. This is because wind-induced NIWs enhance the subinertial velocities u_s and v_s, and thus tidal straining can do more work to NIWs, as inferred from Eq. (9). This is more apparent from the horizontally averaged profiles in Fig. 6c. In case Tide, only 13% of the energy transfer occurs in the mixed layer, while in case Wind_tide it increases to 57%, due to the strong wind-induced near-inertial velocity in the mixed layer.

The instantaneous and cumulative energy transfers averaged between $-400 \le x \le 40$ km are shown in Fig. 5 (black and blue lines). The instantaneous transfer rates are of much smaller magnitudes than those of the wind energy input (Fig. 5a). However, these energy transfer rates from tides are mostly positive, and the cumulative energy inputs from tides are on the same order of magnitude as those from winds (Fig. 5b), indicating that tides can make a considerable contribution to the total near-inertial energy input. As mentioned earlier, the presence of tide-induced NIWs only slightly enhances the energy input from winds. However, the presence

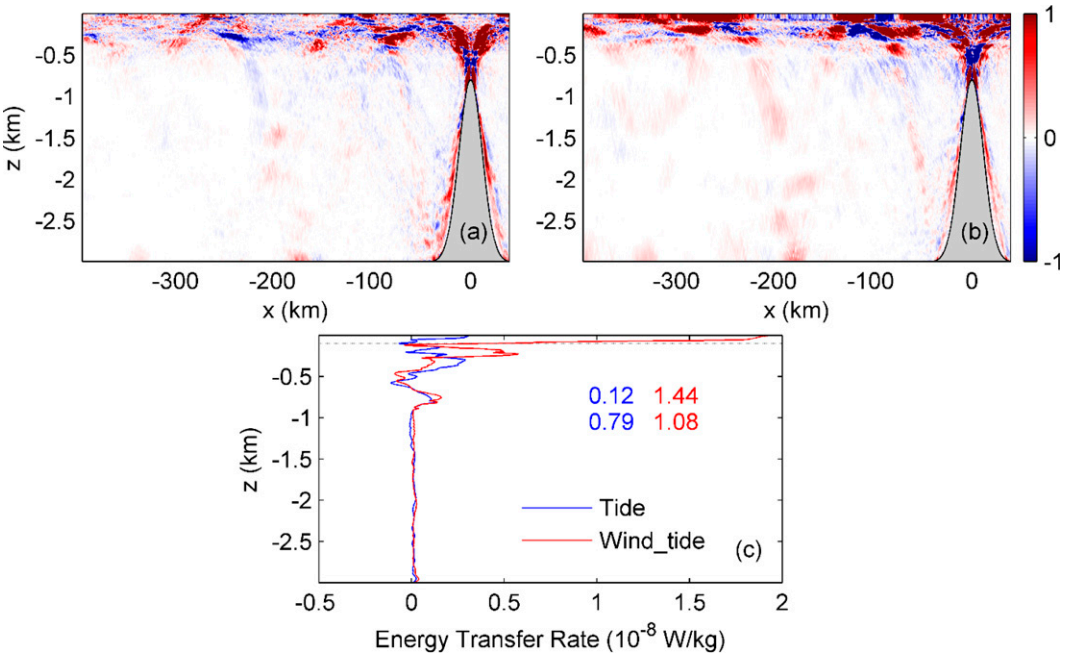

FIG. 6. Energy transfer rate (10^{-8} W kg^{-1}) time-averaged in the last 30 days of simulations for cases (a) Tide and (b) Wind_tide. The color bar is saturated and applies to both (a) and (b). (c) Vertical profiles of the horizontally averaged energy transfer rates in (a) and (b). The upper and lower rows of numbers (10^{-6} W m kg^{-1}) indicate vertical integration of the corresponding profiles (with the same color) above and below the mixed layer depth (gray dashed line), respectively.

of wind-induced NIWs significantly enhances the energy input from tides. By the end of simulations, the cumulative energy input from tides in case Wind_tide (3.42 J m^{-3}) is more than twice the value in case Tide (1.68 J m^{-3}).

Spatial distributions of the energy dissipation rate [Eq. (10)] time-averaged in the last 30 days of simulations are shown in Fig. 7. In case Wind (Fig. 7a), the dissipation is mostly in the surface mixed layer. In case Tide (Fig. 7b), it is concentrated along the internal wave beam and mostly confined in the upper 500-m depth. With the simultaneous presence of wind- and tide-induced NIWs, the dissipation rate is significantly enhanced (Fig. 7c). From the horizontally averaged profiles in Fig. 7d, it is clear that 99% of the dissipation occurs in the mixed layer in case Wind, while 83% of the dissipation is below the mixed layer in case Tide. In case Wind_tide, the dissipation in the mixed layer is about 2 times that below the mixed layer.

The instantaneous energy dissipation rate (Fig. 8a) behaves similarly in cases Wind and Wind_tide and is much larger than that in case Tide. By the end of simulations, the cumulative energy dissipations (Fig. 8b) in cases Wind, Tide, and Wind_tide are 3.96, 1.30, and 6.57 J m^{-3}, respectively. Thus, the simultaneous presence of wind- and tide-induced NIWs dissipates more energy than a linear superposition of the respective dissipation in cases Wind and Tide.

The above energy budget calculations are summarized in Table 1, in which the cumulative W_i and G represent the total energy sources, the cumulative D_s represents the sink, while the resultant E_s and NIE are time-averaged in the last 30 days of simulations. From the second last column, the subharmonic waves mainly consist of NIWs, especially in cases Wind and Wind_tide. Given the many assumptions in deriving Eq. (5) (Hazewinkel and Winters 2011), the neglect of the energy flux divergence term, and the simplifications in calculating G and D_s [Eqs. (9) and (10)], it is a bit surprising that the energy budget for the subharmonic waves closes very well in cases Wind and Wind_tide. It closes to 6.9% and 2.3% of the total energy inputs in these two cases, respectively (the last column in Table 1). In case Tide, the energy budget closes less well, but still acceptable, to within 30% of the total energy input, possibly due to the many assumptions and simplifications in the calculations. The last row shows the effects of the simultaneous presence of wind- and tide-induced NIWs. They mutually enhance each other to extract more energy from wind and tide inputs, respectively. However, this effect is strong for tidal energy input, but weak for wind energy input (51% versus 7%). It should be noted that by definition either tidal or wind energy input is zero in case Wind or Tide, but this does not influence the calculations in the last row of the table. They still provide a reference for comparison that shows the effect of the simultaneous presence of both wind- and tide-induced NIWs in case Wind_tide. The subharmonic and near-inertial energies, as well as the energy dissipation, are all enhanced to a similar degree (20% and 25%). Now it is clear that, of the additional 25% NIE noted in the last section,

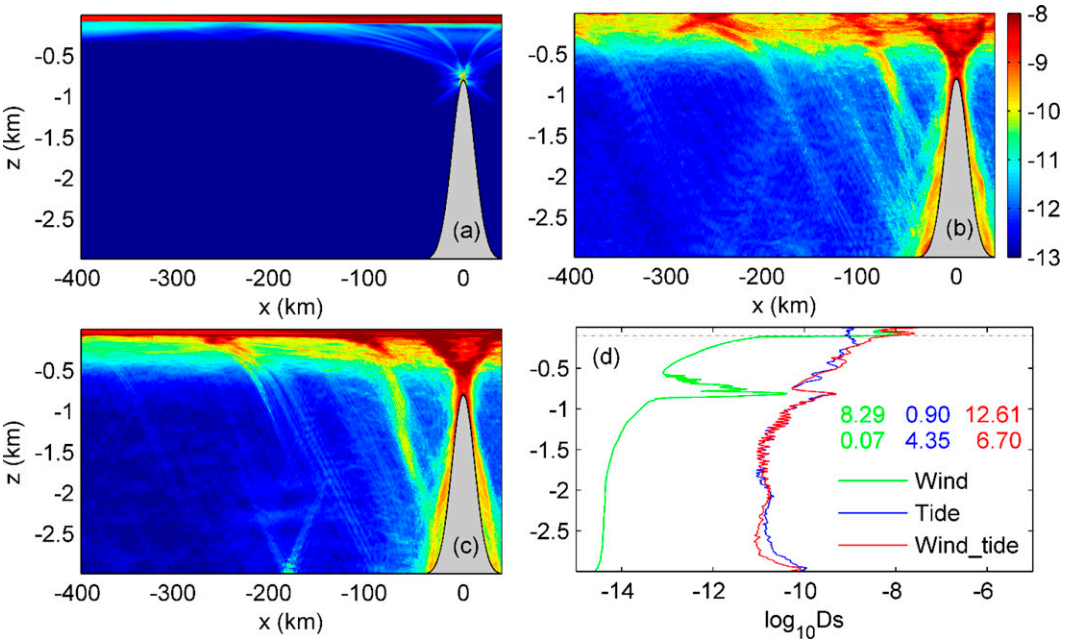

FIG. 7. Logarithm of time-averaged dissipation rate (W kg^{-1}) for cases (a) Wind, (b) Tide, and (c) Wind_tide. The color bar is saturated and applies to (a)–(c). (d) Vertical profiles of the horizontally averaged dissipation rates in (a)–(c). The upper and lower rows of numbers (10^{-7} W m kg^{-1}) indicate vertical integration of the corresponding profiles (with the same color) above and below the mixed layer depth (gray dashed line), respectively.

most of it is contributed by the tides and to a less extent by the wind.

c. *Effects of winds, tides, and topography*

Detailed energy budget calculations are cumbersome, and thus the two ratios R_1 and R_2 [Eqs. (1) and (2)] are used as quick indices to show the enhancement of NIE under different wind, tide, and topographic conditions. When the applied wind stress is multiplied by a factor F_w of 0.2, 0.5, 2, and 5, NIE and R_1 and R_2 are shown in Fig. 9a. Case Tide is the same for different wind intensities and thus NIE_t remains fixed at 0.47 J m^{-3}. As the wind gets stronger, NIE_w and NIE_{wt} increase monotonically. For very weak wind ($F_w = 0.2$), $R_1 = 0$ and no additional NIE is generated. It increases to a maximum of 0.25 at $F_w = 1$ and then decreases slightly with increasing F_w. Thus, the enhancement of NIE (i.e., R_1) seems to saturate with strong wind. With increasing F_w, R_2 decreases monotonically, implying that the importance of tide-induced NIWs diminishes. With increasing tidal excursion ku_0/ω (by increasing u_0), both NIE_t and NIE_{wt} increase monotonically while NIE_w remains fixed (Fig. 9b). For very weak tide, R_1 is close to 0 and the enhancement of NIE is negligible. It increases and then saturates near $R_1 = 0.25$ as ku_0/ω increases. Thus, the enhancement of NIE also saturates with strong tide, which is similar to the effect of the wind. The R_2 increases monotonically, implying that the importance of the tide increases. By keeping the three nondimensional parameters ε, ku_0/ω, and N_0h_0/u_0 the same as those in section 3a (i.e., by changing h_0, u_0, and the topographic width L accordingly), the effect of the normalized ridge height h_0/H is shown in Fig. 9c. The overall behavior is similar to that in Fig. 9b, except that R_1 does not saturate at large h_0/H. For a higher ridge, tide- and wind-induced NIWs are in closer contact, leading to stronger interaction and enhancement of NIE. Of course, h_0/H cannot be increased to 1 and the highest ridge considered is $h_0/H = 0.87$. Since the steepness parameter ε remains unchanged, L is increasing with h_0 and thus the present result is relevant to the ocean where the topographic spectrum is such that taller sills also tend to be wider, which is similar to the situation in Zemskova and Grisouard (2021). Since the interaction between two kinds of NIWs is considered, the phase difference between them might have an effect. The phase of wind-induced NIWs is difficult to adjust since wind forcing is almost a random process. However, the phase of tide-induced NIWs can be adjusted by changing the initial tidal phase ϕ_0. From Fig. 9d, NIE_{wt} and the two ratios are not influenced much by ϕ_0. This shows that the enhancement of NIE is robust under different phase alignments between wind- and tide-induced NIWs.

d. *High NIE near Luzon Strait*

Mixed layer NIE [calculated as $0.5\rho_0(u_i^2 + v_i^2)D$, where D is the mixed layer depth] in the SCS from the hourly GDP dataset is shown in Fig. 10a. The most striking result is that there is high NIE near Luzon Strait. Considering the model results in section 3a, is this due to the mutual enhancement of wind- and tide-induced NIWs in Luzon Strait? Since NIWs usually possess high vertical shear (e.g., Fig. 2d) and are thus conducive to local mixing, and that Luzon Strait is an important gateway of the SCS, the interesting spatial pattern in Fig. 10a might have a potential influence on the Luzon Strait transport

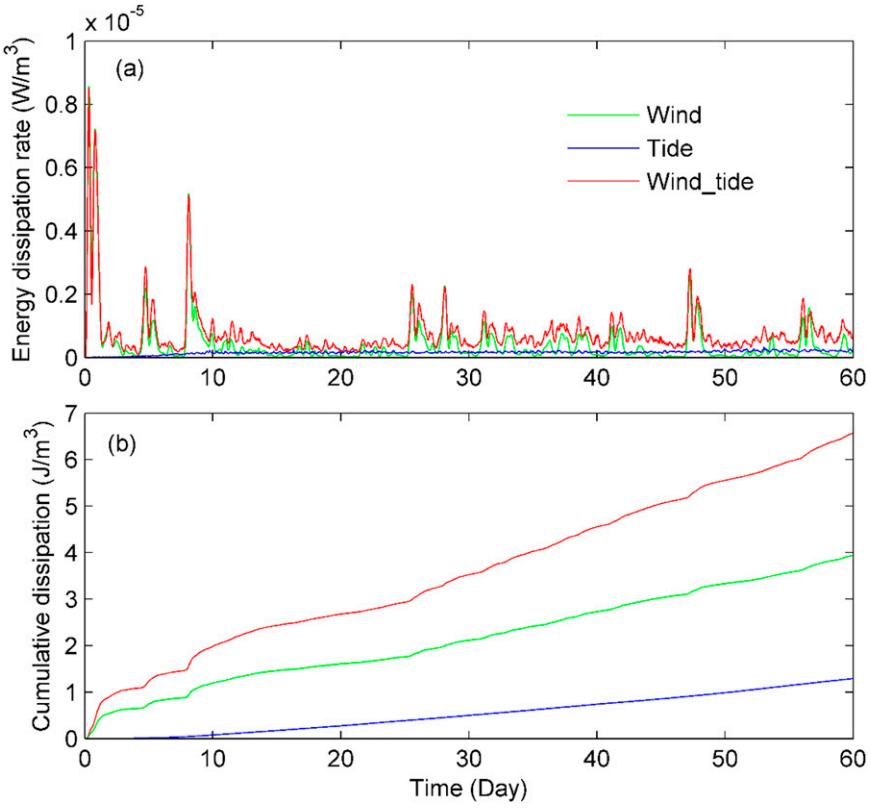

FIG. 8. (a) Instantaneous and (b) cumulative energy dissipation averaged between $-400 \le x \le 40$ km for cases Wind, Tide, and Wind_tide.

(Tian et al. 2006) and even the circulation pattern of the SCS (Gan et al. 2016; Wang et al. 2017).

The annual and winter mean NIE from the hourly GDP dataset averaged between 19° and 22°N are shown in Fig. 10b. The winter mean is overall larger than the annual mean due to the stronger winter wind. The annual mean NIE calculated by Chaigneau et al. (2008) using 3-h-resolution drifter data from July 1999 to December 2006 is also shown (black line). Since the present hourly data have a higher temporal resolution and a much longer time coverage, they generally capture more NIE than that of Chaigneau et al. (2008). The three model results in section 3a are also shown for comparison. Tidal forcing alone can generate only very weak mixed layer NIE. However, wind forcing alone can generate high mixed layer NIE near Luzon Strait, as observed in Fig. 10a. This is due to the stronger wind over Luzon Strait (not shown), e.g., orographic wind jets (Wang et al. 2008). Combined wind and tide forcing further enhances this high NIE pattern. From section 3a, the total tide-induced NIE is comparable to that induced by the wind (0.47 versus 1.10 J m^{-3}). Especially, with the simultaneous presence of wind- and tide-induced NIWs, most of the additional NIE comes from the tide (section 3b). According to Fig. 6c, most of the energy transfer from tides occurs in the mixed layer in the presence of wind forcing, suggesting that wave–wave interactions are important in the mixed layer. The modeled NIE (red line) near Luzon Strait is about three times larger than that of drifter observation (magenta line). Also, the overall slope of the NIE westward decreasing trend from Luzon Strait is much steeper in the model than in drifter observation. This might be because in the

TABLE 1. Energy inputs (J m^{-3}) from wind (W_i) and tide (G) and energy dissipation (D_s) cumulated from the start of simulations; subinertial (E_s) and near-inertial (NIE) energy are time averaged in the last 30 days of simulations.

Case	W_i	G	D_s	E_s	NIE	$\frac{\text{NIE}}{E_s}$	$\frac{W_i + G - D_s - E_s}{W_i + G}$
Wind	5.53	0	3.96	1.19	1.10	92%	6.9%
Tide	0	1.68	1.30	0.88	0.47	53%	−29.8%
Wind_tide	5.97	3.42	6.57	2.60	2.08	80%	2.3%
$\frac{\text{Wind\_tide} - \text{Wind} - \text{Tide}}{\text{Wind\_tide}}$	7%	51%	20%	20%	25%		

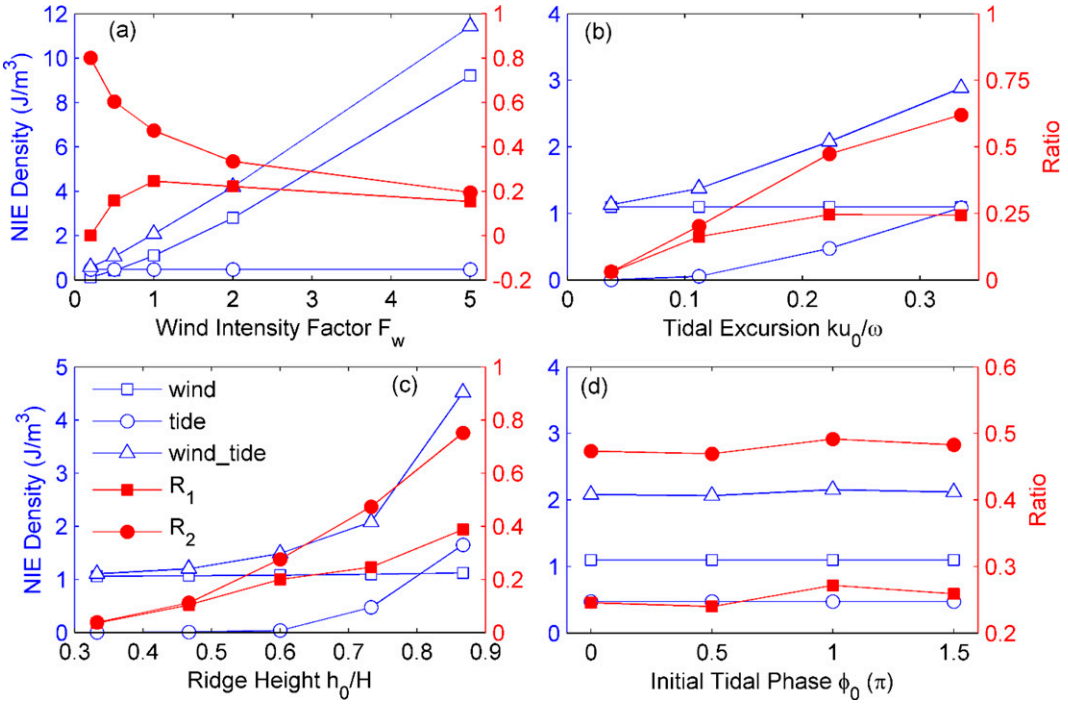

FIG. 9. NIE (left vertical axis) and R_1 and R_2 (right vertical axis) for different (a) wind intensity factors, (b) tidal excursion parameters, (c) ridge heights, and (d) initial tidal phases. Panels (a), (b), and (d) share the same legend as in (c).

present 2D model mesoscale eddies and other complicated background currents are not included, which could disperse or advect mixed layer NIE, thus reducing the too high NIE near Luzon Strait and the westward decreasing slope. Furthermore, drifter observations probably underestimate the actual mixed layer NIE. With more drifter observations and higher time resolution, more NIE might be captured, e.g., compare the orange and black lines in Fig. 10b. Another possible explanation is because the present model is forced by surface wind stress and so it does not take into account current feedback effects. In the ocean, the amount of stress imposed by the wind depends on the relative magnitude and direction of the wind velocity compared with the ocean surface velocity. As was shown by Zhai (2017), the relative wind effect can reduce the net wind energy flux to NIWs by as much as 20%.

One more interesting point to note is that recent results from moorings in Le Boyer et al. (2020) show that, despite sufficient wind forcing, internal waves in the SCS do not exhibit a strong near-inertial peak in the kinetic energy spectrum. This is largely consistent with the small near-inertial peak in our mooring result (black line in Fig. 3). However, by drifter observations in the surface mixed layer, it is shown that there is indeed high NIE near Luzon Strait (Fig. 10a), and this complements mooring results that are usually beneath the surface mixed layer.

4. Conclusions

Wind- and tide-induced NIWs in the northern SCS can mutually enhance each other to generate more NIE. Compared to a linear superposition of wind and tide forcing alone, combined forcing leads to an enhancement of 25% more NIE. This is because in the presence of tide-induced NIWs, the wind can inject more NIE, while in the presence of wind-induced NIWs, tidal straining can transfer more tidal energy to tide-induced NIWs. However, the former effect (more wind energy input) is weak and the latter effect (more tide energy input) contributes most of the additional NIE. In addition to NIE, energy dissipation is also enhanced to a similar degree by the simultaneous presence of wind- and tide-induced NIWs. If tide-induced NIWs are neglected, as is usually the case, the total NIE will be underestimated by almost 50%, which is a significant effect. This mutual enhancement effect between wind- and tide-induced NIWs is similar to the nonlinear coupling between small- and large-scale bathymetry interacting with steady stratified flows, in which the flow response generated by one type of bathymetry can promote more wave generation and dissipation associated with the other type of bathymetry, as reported in the simulations of Klymak (2018) and Zheng et al. (2022).

With increasing wind intensity and tidal excursion, the enhancement of NIE (R_1) saturates, while it increases monotonically with increasing ridge height (up to $h_0/H = 0.87$). A higher ridge leads to a closer contact between wind- and tide-induced NIWs, thus producing stronger mutual enhancement. In the present study, the ridge width also changes with the ridge height, such that the ridge slope remains unchanged. Thus, the present result is relevant to the ocean where the topographic spectrum is such that taller ridges also tend to be wider. The initial tidal phase does not influence the results

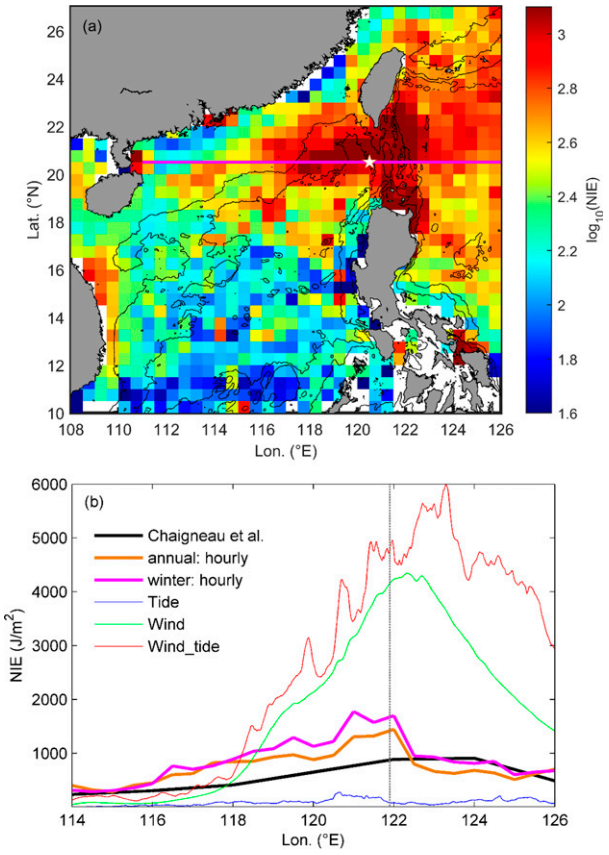

FIG. 10. (a) Logarithm of annual mean mixed layer NIE (J m^{-2}) in the SCS from the hourly GDP dataset. The magenta line is the 20.5°N transect in the model and the white star is the location of the mooring. (b) Annual (orange line) and winter (January–March, magenta line) mean NIE from the hourly dataset, annual mean NIE from Chaigneau et al. (2008, black line), and model mixed layer NIE (blue, green, and red lines). The vertical dotted line indicates the ridge top position in the model.

much, and thus the present results are robust for different wind–tide phase alignments. This result is similar to that in Omidvar et al. (2022), in which it is shown that the presence of wind promotes M_2 internal tide generation in the nearshore region regardless of wind–tide initial phase lag. However, it should be noted that, in the present 2D model, it is relatively easy to get wave–wave energy transfers. In a 3D model, the phases may become randomized enough to damp energy transfers, which will be part of our future research.

For the high mixed layer NIE near Luzon Strait as revealed by satellite-tracked surface drifters, it is mainly generated by the wind while the interaction with tide-induced NIWs can reinforce this pattern. Considering the vertically oscillatory structures (i.e., high vertical shear) of tide-induced NIWs and the mutual enhancement effect, tide-induced NIWs might be important for local mixing and the energetics of NIWs near Luzon Strait.

Acknowledgments. Insightful and constructive comments from Dr. Jody Klymak and two anonymous reviewers greatly help improve the manuscript and are thus gratefully acknowledged. This work was jointly supported by the National Natural Science Foundation of China (91858201, 42130404, 41622601, 42176025, 41776007, 42276022, and 42206012), the Frontier Science Key Research Program of CAS (QYZDJ-SSW-DQC034), GML2019ZD0304 from Southern Marine Science and Engineering Guangdong Laboratory (Guangzhou), the Youth Innovation Promotion Association of CAS (2018378), LTO Independent Research Program (LTOZZ2001 and LTOZZ2205), ISEE2021PY01 from CAS, and the Science and Technology Projects of Guangzhou (202102020897). The numerical simulations are supported by the High Performance Computing Division and HPC managers of Wei Zhou and Dandan Sui in the South China Sea Institute of Oceanology.

Data availability statement. The websites for downloading the satellite-tracked surface drifter and wind stress data are indicated in the main text. The in situ mooring and numerical simulation data can be found at https://figshare.com/articles/dataset/_/15089907.

REFERENCES

Alford, M. H., J. A. MacKinnon, H. L. Simmons, and J. D. Nash, 2016: Near-inertial internal gravity waves in the ocean. *Annu. Rev. Mar. Sci.*, **8**, 95–123, https://doi.org/10.1146/annurev-marine-010814-015746.

Ansong, J. K., and Coauthors, 2018: Geographical distribution of diurnal and semidiurnal parametric subharmonic instability in a global ocean circulation model. *J. Phys. Oceanogr.*, **48**, 1409–1431, https://doi.org/10.1175/JPO-D-17-0164.1.

Chaigneau, A., O. Pizarro, and W. Rojas, 2008: Global climatology of near-inertial current characteristics from Lagrangian observations. *Geophys. Res. Lett.*, **35**, L13603, https://doi.org/10.1029/2008GL034060.

Chen, Z., S. Chen, Z. Liu, J. Xu, J. Xie, Y. He, and S. Cai, 2019: Can tidal forcing alone generate a GM-like internal wave spectrum? *Geophys. Res. Lett.*, **46**, 14 644–14 652, https://doi.org/10.1029/2019GL086338.

D'Asaro, E. A., 1985: The energy flux from the wind to near-inertial motions in the mixed layer. *J. Phys. Oceanogr.*, **15**, 1043–1059, https://doi.org/10.1175/1520-0485(1985)015<1043:TEFFTW>2.0.CO;2.

Elipot, S., R. Lumpkin, R. C. Perez, J. M. Lilly, J. J. Early, and A. M. Sykulski, 2016: A global surface drifter data set at hourly resolution. *J. Geophys. Res. Oceans*, **121**, 2937–2966, https://doi.org/10.1002/2016JC011716.

Gan, J., Z. Liu, and C. Hui, 2016: A three-layer alternating spinning circulation in the South China Sea. *J. Phys. Oceanogr.*, **46**, 2309–2315, https://doi.org/10.1175/JPO-D-16-0044.1.

Garrett, C., and E. Kunze, 2007: Internal tide generation in the deep ocean. *Annu. Rev. Fluid Mech.*, **39**, 57–87, https://doi.org/10.1146/annurev.fluid.39.050905.110227.

Hazewinkel, J., and K. B. Winters, 2011: PSI of the internal tide on a β plane: Flux divergence and near-inertial wave propagation. *J. Phys. Oceanogr.*, **41**, 1673–1682, https://doi.org/10.1175/2011JPO4605.1.

Hibiya, T., M. Nagasawa, and Y. Niwa, 2002: Nonlinear energy transfer within the oceanic internal wave spectrum at mid

and high latitudes. *J. Geophys. Res.*, **107**, 3207, https://doi.org/10.1029/2001JC001210.

Hu, Q., X. Huang, Z. Zhang, X. Zhang, X. Xu, H. Sun, C. Zhou, W. Zhao, and J. Tian, 2020: Cascade of internal wave energy catalyzed by eddy-topography interactions in the deep South China Sea. *Geophys. Res. Lett.*, **47**, e2019GL086, https://doi.org/10.1029/2019GL086510.

Klymak, J. M., 2018: Nonpropagating form drag and turbulence due to stratified flow over large-scale abyssal hill topography. *J. Phys. Oceanogr.*, **48**, 2383–2395, https://doi.org/10.1175/JPO-D-17-0225.1.

Lamb, K. G., 2004: Nonlinear interaction among internal wave beams generated by tidal flow over supercritical topography. *Geophys. Res. Lett.*, **31**, L09313, https://doi.org/10.1029/2003GL019393.

Large, W. G., J. C. McWilliams, and S. C. Doney, 1994: Oceanic vertical mixing: A review and a model with a nonlocal boundary layer parameterization. *Rev. Geophys.*, **32**, 363–403, https://doi.org/10.1029/94RG01872.

Le Boyer, A., M. H. Alford, R. Pinkel, T. D. Hennon, Y. J. Yang, D. Ko, and J. Nash, 2020: Frequency shift of near-inertial waves in the South China Sea. *J. Phys. Oceanogr.*, **50**, 1121–1135, https://doi.org/10.1175/JPO-D-19-0103.1.

Liang, X., and C. Wunsch, 2015: Note on the redistribution and dissipation of tidal energy over mid-ocean ridges. *Tellus*, **67A**, 27385, https://doi.org/10.3402/tellusa.v67.27385.

Liu, Y., Z. Jing, and L. Wu, 2019: Wind power on oceanic near-inertial oscillations in the global ocean estimated from surface drifters. *Geophys. Res. Lett.*, **46**, 2647–2653, https://doi.org/10.1029/2018GL081712.

MacKinnon, J. A., and K. B. Winters, 2005: Subtropical catastrophe: Significant loss of low-mode tidal energy at 28.9 degrees. *Geophys. Res. Lett.*, **32**, L15605, https://doi.org/10.1029/2005GL023376.

Marshall, J., A. Adcroft, C. Hill, L. Perelman, and C. Heisey, 1997: A finite-volume, incompressible Navier-Stokes model for studies of the ocean on parallel computers. *J. Geophys. Res.*, **102**, 5753–5766, https://doi.org/10.1029/96JC02775.

Müller, P., G. Holloway, F. Henyey, and N. Pomphrey, 1986: Nonlinear interactions among internal gravity waves. *Rev. Geophys.*, **24**, 493–536, https://doi.org/10.1029/RG024i003p00493.

Munk, W. H., 1981: Internal waves and small-scale processes. *Evolution of Physical Oceanography: Scientific Surveys in Honor of Henry Stommel*, B. A. Warren and C. Wunsch, Eds., MIT Press, 264–291.

Nagai, T., A. Tandon, E. Kunze, and A. Mahadevan, 2015: Spontaneous generation of near-inertial waves by the Kuroshio Front. *J. Phys. Oceanogr.*, **45**, 2381–2406, https://doi.org/10.1175/JPO-D-14-0086.1.

Nikurashin, M., and R. Ferrari, 2010: Radiation and dissipation of internal waves generated by geostrophic motions impinging on small-scale topography: Theory. *J. Phys. Oceanogr.*, **40**, 1055–1074, https://doi.org/10.1175/2009JPO4199.1.

——, and S. Legg, 2011: A mechanism for local dissipation of internal tides generated at rough topography. *J. Phys. Oceanogr.*, **41**, 378–395, https://doi.org/10.1175/2010JPO4522.1.

Omidvar, S., M. Fagundes, and C. B. Woodson, 2022: Modification of internal wave generation and energy conversion in the nearshore due to tide-tide and tide-wind interactions. *J. Geophys. Res. Oceans*, **127**, e2021JC017986, https://doi.org/10.1029/2021JC017986.

Onuki, Y., and T. Hibiya, 2015: Excitation mechanism of near-inertial waves in baroclinic tidal flow caused by parametric subharmonic instability. *Ocean Dyn.*, **65**, 107–113, https://doi.org/10.1007/s10236-014-0789-3.

Pollard, R. T., and R. C. Millard, 1970: Comparison between observed and simulated wind-generated inertial oscillations. *Deep-Sea Res.*, **17**, 153–175, https://doi.org/10.1016/0011-7471(70)90043-4.

Sugiyama, Y., Y. Niwa, and T. Hibiya, 2009: Numerically reproduced internal wave spectra in the deep ocean. *Geophys. Res. Lett.*, **36**, L07601, https://doi.org/10.1029/2008GL036825.

Tian, J., Q. Yang, X. Liang, L. Xie, D. Hu, F. Wang, and T. Qu, 2006: Observation of Luzon Strait transport. *Geophys. Res. Lett.*, **33**, L19607, https://doi.org/10.1029/2006GL026272.

Tort, M., and K. Winters, 2018: Poleward propagation of near-inertial waves induced by fluctuating winds over a baroclinically unstable zonal jet. *J. Fluid Mech.*, **834**, 510–530, https://doi.org/10.1017/jfm.2017.698.

Vanneste, J., 2013: Balance and spontaneous wave generation in geophysical flows. *Annu. Rev. Fluid Mech.*, **45**, 147–172, https://doi.org/10.1146/annurev-fluid-011212-140730.

Wang, G., D. Chen, and J. Su, 2008: Winter eddy genesis in the eastern South China Sea due to orographic wind jets. *J. Phys. Oceanogr.*, **38**, 726–732, https://doi.org/10.1175/2007JPO3868.1.

Wang, S., A. Cao, X. Chen, Q. Li, and J. Song, 2021a: On the resonant triad interaction over mid-ocean ridges. *Ocean Modell.*, **158**, 101734, https://doi.org/10.1016/j.ocemod.2020.101734.

——, ——, X. Liang, X. Chen, and J. Meng, 2021b: Impact of background geostrophic currents with vorticity on resonant triad interaction over midocean ridges. *J. Geophys. Res. Oceans*, **126**, e2021JC017227, https://doi.org/10.1029/2021JC017227.

Wang, X., Z. Liu, and S. Peng, 2017: Impact of tidal mixing on water mass transformation and circulation in the South China Sea. *J. Phys. Oceanogr.*, **47**, 419–432, https://doi.org/10.1175/JPO-D-16-0171.1.

Xie, X., X. Shang, H. van Haren, and G. Chen, 2011: Observations of parametric subharmonic instability-induced near-inertial waves equatorward of the critical diurnal latitude. *Geophys. Res. Lett.*, **38**, L05603, https://doi.org/10.1029/2010GL046521.

Xing, J., and A. M. Davies, 1997: The influence of wind effects upon internal tides in shelf edge regions. *J. Phys. Oceanogr.*, **27**, 2100–2125, https://doi.org/10.1175/1520-0485(1997)027<2100:TIOWEU>2.0.CO;2.

——, and ——, 2002: Processes influencing the non-linear interaction between inertial oscillations, near inertial internal waves and internal tides. *Geophys. Res. Lett.*, **29**, 1067, https://doi.org/10.1029/2001GL014199.

Yang, W., T. Hibiya, Y. Tanaka, L. Zhao, and H. Wei, 2018: Modification of parametric subharmonic instability in the presence of background geostrophic currents. *Geophys. Res. Lett.*, **45**, 12 957–12 962, https://doi.org/10.1029/2018GL080183.

Young, W. R., Y.-K. Tsang, and N. J. Balmforth, 2008: Near-inertial parametric subharmonic instability. *J. Fluid Mech.*, **607**, 25–49, https://doi.org/10.1017/S0022112008001742.

Zemskova, V. E., and N. Grisouard, 2021: Near-inertial dissipation due to stratified flow over abyssal topography. *J. Phys. Oceanogr.*, **51**, 2483–2504, https://doi.org/10.1175/JPO-D-21-0007.1.

Zhai, X., 2017: Dependence of energy flux from the wind to surface inertial currents on the scale of atmospheric motions. *J. Phys. Oceanogr.*, **47**, 2711–2719, https://doi.org/10.1175/JPO-D-17-0073.1.

——, R. J. Greatbatch, and C. Eden, 2007: Spreading of near-inertial energy in a 1/12° model of the North Atlantic Ocean. *Geophys. Res. Lett.*, **34**, L10609, https://doi.org/10.1029/2007GL029895.

Zhang, Z., W. Zhao, B. Qiu, and J. Tian, 2017: Anticyclonic eddy sheddings from Kuroshio loop and the accompanying cyclonic eddy in the northeastern South China Sea. *J. Phys. Oceanogr.*, **47**, 1243–1259, https://doi.org/10.1175/JPO-D-16-0185.1.

Zheng, K., M. Nikurashin, and J. Tian, 2022: Non-local energy dissipation of lee waves and turbulence in the South China Sea. *J. Geophys. Res. Oceans*, **127**, e2021JC017877, https://doi.org/10.1029/2021JC017877.